buildings

MDPI

Article

Design and Operation of a Novel Cross Fin in Hot-Water Production System for Buildings

Qiang Cui [1,2,*], Tao Ning [3,4], Chuanqing Huang [5], Chunyan Wu [1,2] and Junwei Su [3,*]

[1] School of Petroleum Engineering and Environmental Engineering, Yan'an University, Yan'an 716000, China; yauwcy@yau.edu.cn
[2] Engineering Research Center of Efficient Exploitation of Oil and Gas Resources and Protection Ecological Environment, Universities of Shaanxi Province, Yan'an 716000, China
[3] School of Human Settlements and Civil Engineering, Xi'an Jiaotong University, Xi'an 710049, China; ningtao9226@sxycpc.com
[4] Zhidan Oil Production Plant of Yanchang Oilfield Co., Ltd., Yan'an 716000, China
[5] College of Chemistry and Chemical Engineering, Shaanxi University of Science & Technology, Xi'an 710021, China; huangcq@sust.edu.cn
* Correspondence: cuiqiang227@sohu.com (Q.C.); sujunwei@xjtu.edu.cn (J.S.)

Abstract: The importance of phase change heat storage (PCHS) in solar thermal applications is limited by the low thermal conductivity of phase change materials (PCMs) and the uneven temperature distribution during heat transfer. This study proposes to use composite fins for heat exchange in the PCHS module and integrate them into a hot-water production system (HWPS) for building heating. The effectiveness of the novel fin structure is assessed through thorough numerical simulations and experimental validation. An examination of melting fractions, temperature distribution, and flow characteristics of the molten PCMs across various fin structures indicates that increasing the lengths and quantities of the cross fins can alleviate the challenge of incomplete melting at the end of the charging process. Notably, expanding the surface area of the cross fins results in a 7.37-fold increase in the average thermal storage rate and a 781.25% enhancement in the average temperature response compared to the original design. These findings show that the new composite fin design greatly improves the heat storage performance of an HWPS, which is of great significance for building energy conservation.

Keywords: energy storage; melting rate; cross fin; enhancement of heat transfer; numerical simulation

Academic Editors: Francesco Nocera and Antonio Caggiano

Received: 25 December 2024
Revised: 11 January 2025
Accepted: 16 January 2025
Published: 22 January 2025

Citation: Cui, Q.; Ning, T.; Huang, C.; Wu, C.; Su, J. Design and Operation of a Novel Cross Fin in Hot-Water Production System for Buildings. *Buildings* **2025**, *15*, 320. https://doi.org/10.3390/buildings15030320

1. Introduction

With the rapid growth of global energy demand and the increasingly severe climate change, the development of sustainable energy systems has become the primary focus of all countries [1,2]. In this context, building energy storage is an important part of the distributed energy system [3,4], and its development is closely related to the change in the global energy pattern [5,6].

Thermal energy storage, an advanced technology in energy storage and management, plays a crucial role in building heating applications, particularly in enhancing energy efficiency [7,8], ensuring consistent heating quality, and advancing the use of renewable energy sources [9,10]. Phase change materials (PCMs) are essential components in thermal energy storage systems, serving as adaptable heat storage mediums that can be seamlessly incorporated into various energy systems [11–13] and showcasing extensive possibilities for applications [14,15]. In order to improve the speed of the phase change energy storage

process, strategies such as adding fins [16,17] and metal foam [18,19], altering packaging methods [20–22], and introducing nanomaterials [23,24] can be adopted.

Fins are widely used in various heat exchangers to enlarge heat transfer areas, as well as to promote fluid mixing, thus improving heat transfer efficiency [25,26]. Earlier research has demonstrated that fins are capable of enhancing the thermal efficiency of PCMs [27]. Guo et al. [28] put forward a curved structure derived from a straight fin. The non-uniform arrangement of fins has led to an improved melting performance, ranging from 24.5% to 9.2% compared with the uniform arrangement. Xu et al. [29] demonstrated that the use of an intelligent fin for PCMs in a cavity results in a 28.6% reduction in the melting time. In the work of Boujelbene et al. [30], both the melting and solidification features of PCMs in a horizontal double-tube unit with twisted fins are investigated, demonstrating a 10% and 14% increase in charge and discharge rates, respectively. Mills et al. [31] explored the enhancement of the melting process using a naturally inspired tree structure, which resulted in a 17% reduction in heater temperature when heated from the side.

Unnikrishnan et al. [32] investigate the performance of the internal corrugated structure using simulations and experimentations. The increase in the convective heat transfer rate and slope results in improved PV performance. Han et al. [33] conducted experiments on the application of a copper fin thermochemical reactor in the construction industry. The copper fin reactor demonstrates a faster temperature rise during loading owing to enhanced heat transfer. Specifically, the outlet air temperature of the copper fin reactor reached 158.7 °C in 2.88 h, signifying a 25.9% increase. Guedri et al. [34] employed different spiral fins with varying fin numbers and lengths to create equal heat transfer surfaces under different conditions. The double fin and triple fin showed the best performance, shortening the solidification process by 15.87% and 30.43%. In a study conducted by Liu et al. [35], a new bionic spider web fin was designed. The full melting time for the accumulator with the new web fin is only 48 s, in contrast to 140 s for the radial fin, signifying a significantly longer duration.

Yang et al. [36] explored the impact of variable-speed rotation on TES devices. They noted that a variable speed for rotation resulted in better melting performance. In comparison with constant velocity, phase change time is reduced by 17.37%, while the mean heat charging rate increases significantly, by 22.72%. Mao et al. [37] analyze the potential of a truncated cone structure for enhancing the melting process. They argue that the truncated cone structure performs best during the melting procedure. Kirincic et al. [38] explore the installation of longitudinal fins upon tubes to enhance heat storage performance compared with conventional tube configuration. Their study finds that the overall heat transfer effect notably improves post-installation of the fin during the thermal loading and unloading cycle, achieving a 52% and 43% time saving compared to the ordinary tube configuration. Mudhafar et al. [39] compare the three-way fin shape to the conventional longitudinal fin shape. They reveal that while the PCM without adding fins melts about 15% after 6 h, the PCM using three-way fins melts completely after 3.5 h, achieving a 33% time-saving ratio. Prior research has suggested enhancing energy efficiency or increasing the melting rate of PCM by altering the fin shape, distribution position, and rotation. There is a gap in the research concerning fin shape within the context of enhanced heat transfer. While active enhanced heat transfer can significantly improve the overall heat transfer performance of the PCHS system, its application is hindered by the substantial requirement for external electric energy. On the other hand, the metal fin, known for its simple installation and exceptional performance, plays a crucial role in enhancing heat transfer in the PCHS system. Strategies to mitigate the adverse effects of the fin on overall heat charging, while maintaining a high thermal charging rate, necessitate further exploration and discussion.

In this paper, we propose to use composite fins for heat exchange in the PCHS module and integrate them into a building heating and hot-water production system (HWPS). The research involves the design and evaluation of nine fin configurations to determine the most effective structure for reducing the non-uniformity of phase change melting. The contents of the study include (1) theoretical modeling and simulation of thermofluidic properties using advanced computational fluid dynamics tools (ANSYS FLUENT 2021) to analyze the impact of geometric parameters on the system; (2) a detailed examination of fin design to compare melting rates, temperature profiles, and flow patterns at different locations and heat absorption levels; and (3) a comparative analysis of the properties of the new cross structure against the conventional design in enhancing the heat transfer efficiency of the HWPS.

2. Problem Formulation

2.1. Physical Model

Figure 1 shows the schematic diagram of the solar heat storage system used for building heating. It is composed of a hot-water production system, a phase change heat storage system (PCHSS), and a building energy system. The PCHSS uses solar energy for photothermal conversion to provide continuous heating for the building. This study delves into the PCHSS module outlined in Figure 2. Noteworthy is the overall length of the tank, measuring 500 mm, comprising various curved fins and a singular ring fin to create a novel fin structure. The thickness of the tube wall is set at 1 mm, with the inner tube facilitating the movement of high-temperature fluid powered by solar energy. Because of the high thermal conductivity of copper, the PCHSS is simplified into a two-dimensional cross-section for analysis. The inner radii (r_1) and outer radii (r_2) of the shell are 10 mm and 50 mm, respectively. Nine innovative ring fins were manufactured, the cross-section of which is shown in Figure 3. Figure 3a–c depict Cases 1–3, while Figure 3d–f show Cases 4–6. In addition, Figure 3g–i show Cases 7–9, integrating the different annular fin radii and number of fins, whose respective geometric specifications are listed in Table 1. Furthermore, thermophysical parameters of the RT50 paraffin employed in the PCHSS are outlined in Table 2, with the use of RT82 paraffin specified to authenticate the subsequent numerical model.

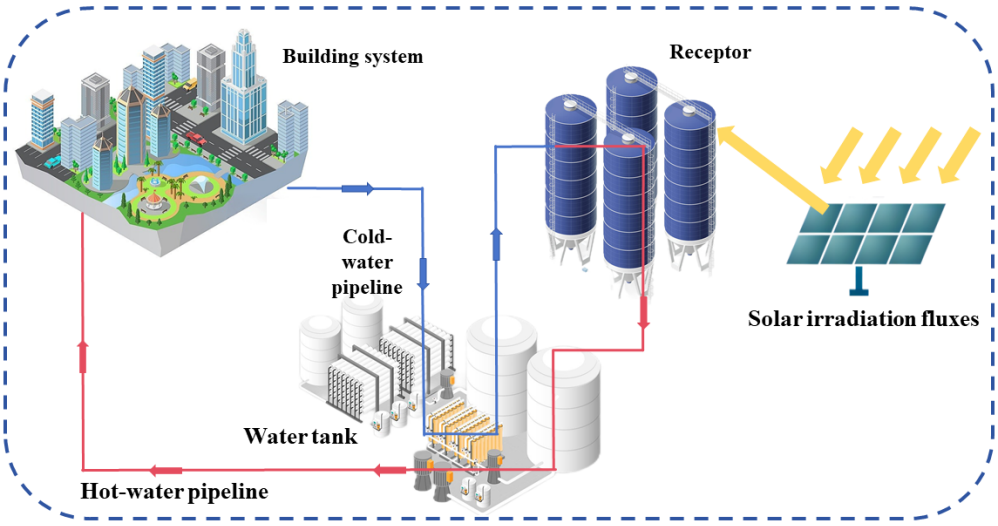

Figure 1. Solar heat storage system used for building heating.

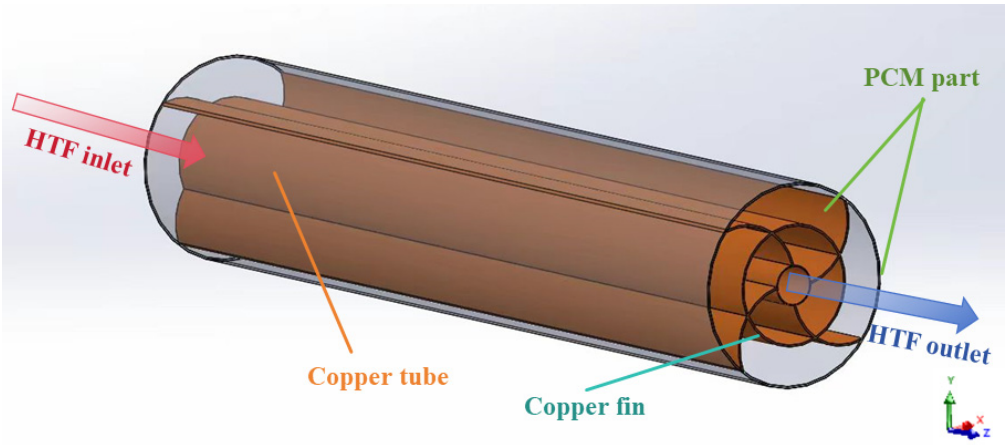

Figure 2. Schematic of the unit structure for PCHSS.

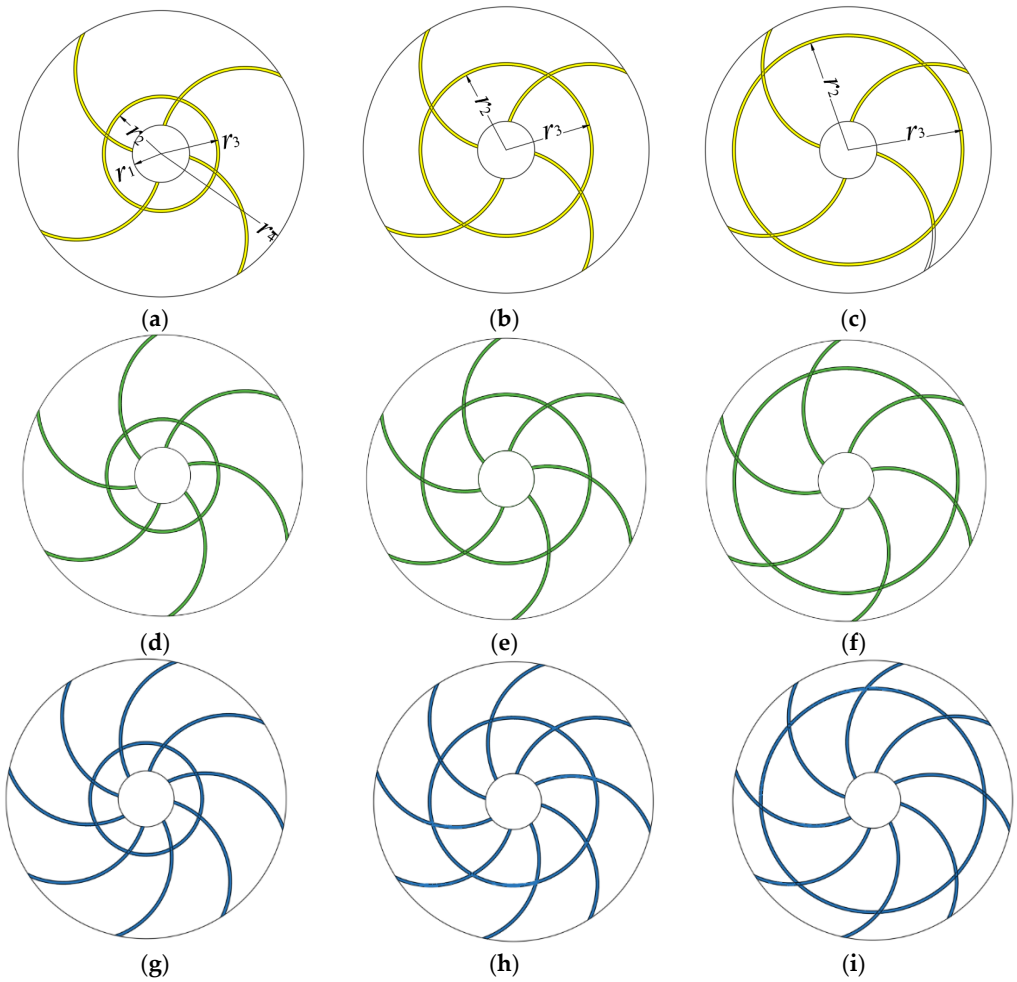

Figure 3. Schematic of cross fin design structure with different positions for inner circular fin: (**a**–**c**) 4 curved fins +1 circular fin of different radii; (**d**–**f**) 6 curved fins +1 circular fin of different radii; (**g**–**i**) 8 curved fins +1 circular fin of different radii.

Table 1. Geometric structure classification of Cases 1–9.

	Inside Diameter of Circular Fin (r_2)	Outer Diameter of Circular Fin (r_3)	Curvature of the Curved Fin	Number of Curved Fins
Case 1	19.5 mm	20.5 mm	30°	4
Case 2	29.5 mm	30.5 mm	30°	4
Case 3	39.5 mm	40.5 mm	30°	4
Case 4	19.5 mm	20.5 mm	30°	6
Case 5	29.5 mm	30.5 mm	30°	6
Case 6	39.5 mm	40.5 mm	30°	6
Case 7	19.5 mm	20.5 mm	30°	8
Case 8	29.5 mm	30.5 mm	30°	8
Case 9	39.5 mm	40.5 mm	30°	8

Table 2. Thermophysical properties of PCMs adapted from [40,41].

Property	Paraffin RT50	Paraffin RT82	Cu	Unit
Thermal conductivity (k)	0.2	0.2	387.6	W/m·K
Melting temperature (T_m)	321.15	353.15		K
Volumetric coefficient of thermal expansion (β)	0.0006	0.001		K^{-1}
Solidus temperature (T_s)	318.15	351.15		K
Liquidus temperature (T_l)	324.15	355.15		K
Latent heat of fusion (λ)	168,000	176,000		J/kg
Dynamic viscosity (μ)	0.0048	0.03499		Pa·s
Isobaric specific heat (c_p)	2000	2000	381	J/kg·K
Density (ρ)	880 (solid) 760 (liquid)	950 (solid) 770 (liquid)	8978	Kg/m^3

2.2. Mathematical Model

To address the transient problem, numerical implementations are made with assumptions such as [42]:

(1) PCMs and copper have fixed parameters of conductivity, specific heat, and others. They are invariant with temperature changes;
(2) All the fluid flow described in this study is incompressible;
(3) A Boussinesq model is utilized to describe the local free convective heat transfer;
(4) The phase transition process does not take into account heat loss and radiation with the outside world.

Governing equations are [43,44]:

Continuity equation (used to describe the mass conservation of a fluid during a phase transition) [45]:

$$\frac{\partial u}{\partial x} + \frac{\partial v}{\partial y} = 0 \tag{1}$$

Momentum equation (describing hydrodynamic properties and natural convection effects):

$$\frac{\partial(\rho u)}{\partial t} + \frac{\partial(\rho uu)}{\partial x} + \frac{\partial(\rho uv)}{\partial y} = -\frac{\partial p}{\partial x} + \frac{\partial}{\partial x}\left(\mu\frac{\partial u}{\partial x}\right) + \frac{\partial}{\partial y}\left(\mu\frac{\partial u}{\partial y}\right) + A_{mush}\frac{(1-f_m)^2}{f_m^3+\varepsilon}u \tag{2}$$

$$\begin{aligned}&\tfrac{\partial(\rho v)}{\partial t} + \tfrac{\partial(\rho uv)}{\partial x} + \tfrac{\partial(\rho vv)}{\partial y} = \\ &-\tfrac{\partial p}{\partial y} + \tfrac{\partial}{\partial x}\left(\mu\tfrac{\partial v}{\partial x}\right) + \tfrac{\partial}{\partial y}\left(\mu\tfrac{\partial v}{\partial y}\right) + A_{mush}\tfrac{(1-f_m)^2}{f_m^3+\varepsilon}v + \rho g\beta(T-T_m)\end{aligned} \tag{3}$$

Energy equation (captures heat transfer and latent heat behavior of phase transitions):

$$\frac{\partial \rho h}{\partial t} + \nabla \cdot (\rho v h) = \frac{\partial}{\partial x}\left(k\frac{\partial T}{\partial x}\right) + \frac{\partial}{\partial y}\left(k\frac{\partial T}{\partial y}\right) \tag{4}$$

where A_{mush} takes the value of 10^5 kg/m^3 [46]. ε is the numerical constant allowing the non-zero mathematical operations. f_m is the liquid fraction determined by:

$$f_m = \begin{cases} 0, & T \le T_s \\ \frac{T-T_s}{T_l-T_s}, & T_s < T < T_l \\ 1, & T \ge T_l \end{cases} \tag{5}$$

$\dot{f_m}$ is melting rate:

$$\dot{f_m} = \frac{\partial f}{\partial t} \tag{6}$$

The total enthalpy is h:

$$h = h_{sen} + h_{lat} \tag{7}$$

$$h_{sen} = h_{ref} + \int_{T_{ref}}^{T} c_p dT \tag{8}$$

$$h_{lat} = f\lambda \tag{9}$$

The amount of heat absorbed is [44]:

$$Q_s = mc_p(T_c - T_i) \tag{10}$$

$$Q_l = m\lambda f \tag{11}$$

$$Q = Q_s + Q_l \tag{12}$$

Instantaneousness and average manipulation yield thermal storage rates by [47]:

$$\dot{q} = \frac{\partial Q}{\partial t} \tag{13}$$

$$\overline{q} = \frac{\partial Q_m}{\partial t_m} \tag{14}$$

2.3. Initial and Boundary Conditions

Initial and boundary conditions:

$$t = 0,\ T_i = 300.15\ \text{K} \tag{15}$$

$$r = R_1 = 10\ \text{mm},\ T = T_w = 348.15\ \text{K} \tag{16}$$

Thermal interface between copper fins and PCMs:

$$T_{fin}\,|_\Omega = T_{pcm}\,|_\Omega \tag{17}$$

$$-\lambda_{fin}\frac{\partial T_{fin}}{\partial \vec{n}}\bigg|_\Omega = -\lambda_{pcm}\frac{\partial T_{pcm}}{\partial \vec{n}}\bigg|_\Omega \tag{18}$$

3. Numerical Procedure and Validation

3.1. Meshing and Numerical Procedure

The melting process is simulated using ANSYS FLUENT 2021. Aiming to simulate the actual scenario more accurately, grid partitioning is conducted using ICEM 2021 software, and fine encryption processing is specifically applied to the fin heat transfer boundary. The fin and the external PCM are divided into two different areas for the subsequent setting of physical quantities. A detailed grid diagram of this process is illustrated in Figure 4, establishing a robust database for subsequent analysis. The discretization employs the second-order upwind scheme. SIMPLE arithmetic manipulation is utilized to solve the pressure–velocity coupling problem. The PRESTO! algorithm corrects pressure updates during each round of iteration, within which 10^{-9} is the key to the convergence standard [48,49].

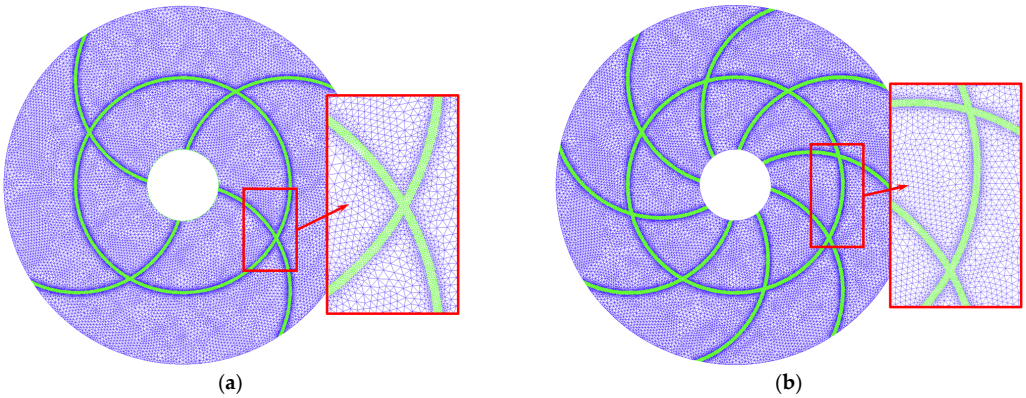

Figure 4. Representative mesh for two cases with different inner fin radii: (**a**) meshing for Case 2; (**b**) meshing for Case 8.

3.2. Independence of Mesh and Time Step

Verification and analysis of the number of meshes and the time steps in the numerical procedure were conducted. The maximum limit of global elements is set at 0.2, 0.3, and 0.4, resulting in 52,382, 88,368, and 136,334 grid nodes, respectively. Time steps are chosen as 0.04 s, 0.05 s, and 0.06 s to explore their impact on the liquid fraction during melting, as illustrated in Figure 5. The influence of the number of meshes and time steps upon the melting fraction demonstrates that mesh count surpassing 88,368 results in a 6.04% deduction in the liquid fraction, while a time step below 0.05 s achieves a 20.14% decrease (see Figure 5). The subsequent study employs a time step of 0.05 s and mesh count of 88,368.

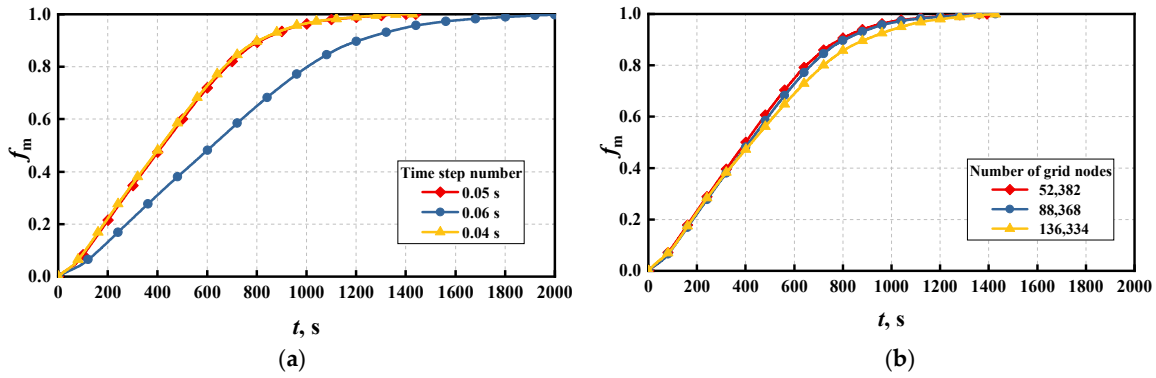

Figure 5. Independence examination on different numbers of: (**a**) meshes; (**b**) time steps.

3.3. Model Verification

To confirm the validity of this numerical model, we conduct model verification using the experimental data of Abidi et al. [50]. The operation in the numerical study is consistent with the experimental scenario in reference [50]. Paraffin RT82 as shown in Table 1 is used as a phase change material. The initial temperature is 300 K, and the inner wall temperature is 350 K. Figure 6 describes the comparison of the mean temperature of PCM between these two approaches. The errors in the numerical calculation are analyzed. Comparative analysis shows that the deviation between the two is 2.85%, which is caused by the inevitable heat loss in the experiment. It can be shown that the numerical model has strong feasibility.

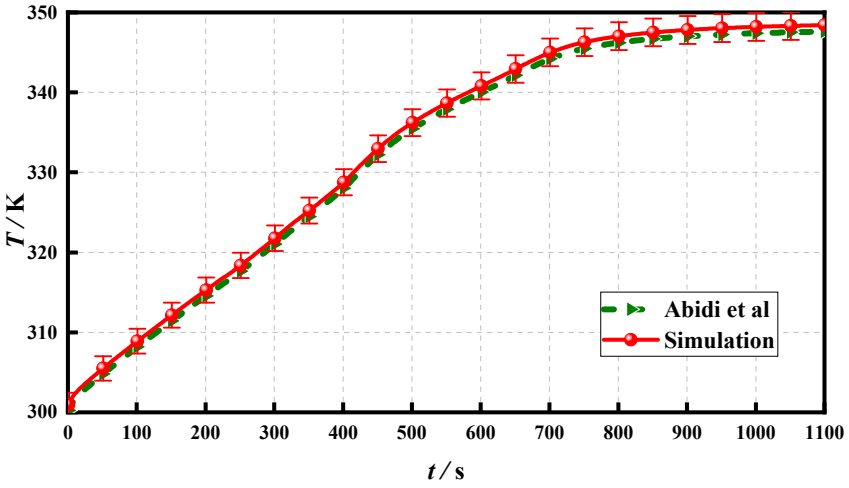

Figure 6. Model verification of mean temperature of PCM.

4. Results and Discussion

4.1. Comparative Analysis of Melting Performance

While analyzing the liquid fraction distribution, temperature changes, and fluid flow characteristics of Cases 1–9, the melting states corresponding to different time points are examined through a detailed comparison of melting discrepancies. The liquid phase distribution diagram (Figure 7), temperature variation diagram (Figure 8), and velocity distribution diagram (Figure 9) are presented individually. From Figures 7 and 8, it is evident that, during the initial melting phase, the inner tube first heats its adjacent PCM and fins. Owing to excellent conductivity, cross fins facilitate rapid heat transfer. In Cases 1–3, the fin number remains unchanged, while the radius of the annular fin varies from 20 mm to 30 mm and 40 mm, respectively. At t = 780 s and t = 1020 s, the PCM distribution within the cell becomes more uniform with increasing annular fin diameter, enhancing internal heat exchange efficiency. As time progresses to late melting at t = 1200 s, a region forms at the bottom thanks to the influence of buoyancy flow in the upper region. Nevertheless, with an increase in annular fin radius, these challenging-to-melt regions decrease. Notably, the low-temperature PCM is substantially reduced in Case 3. At 1500 s, the challenging-to-melt region in Case 3 exists only at the bottom, while in Case 1 and Case 2, these regions also persist on the left and right of the PCM.

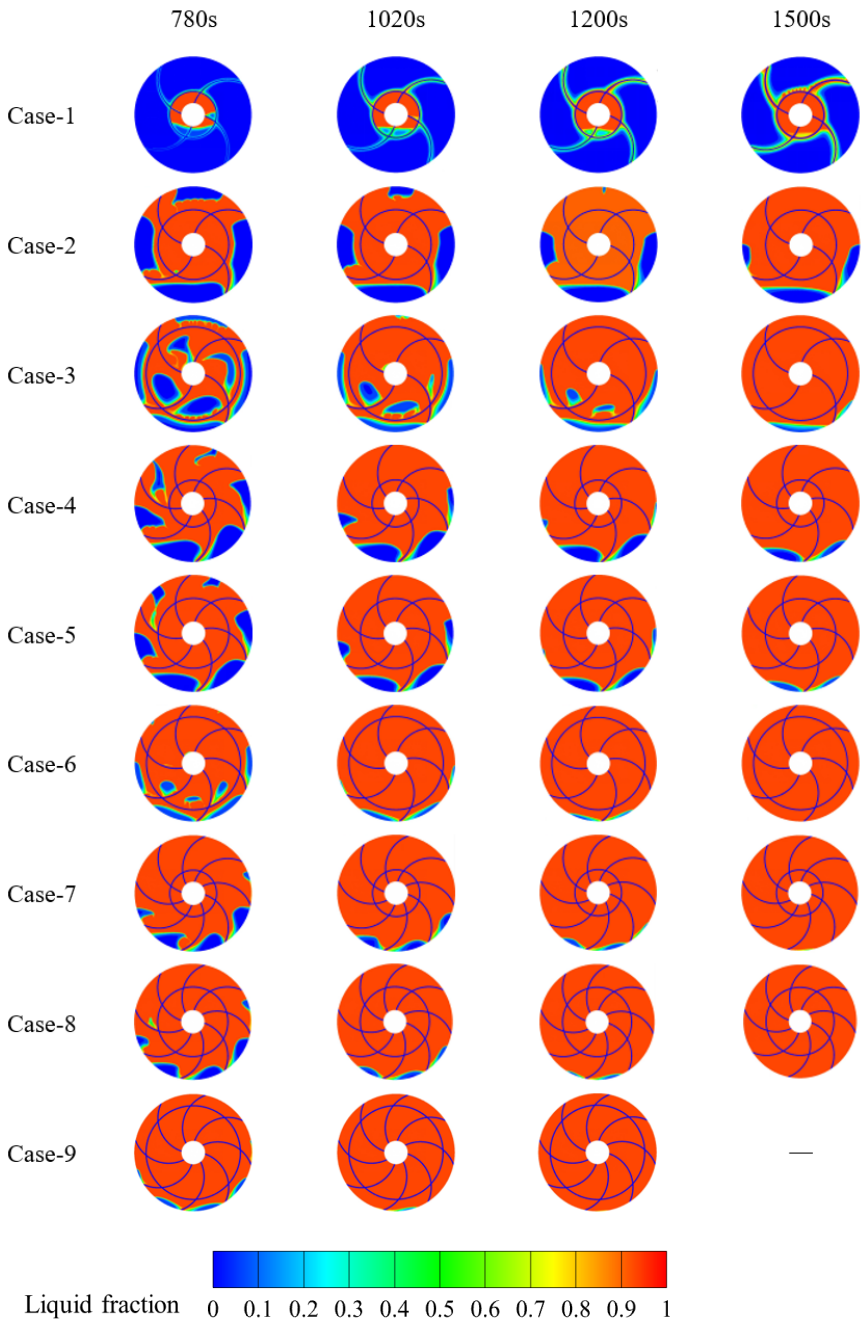

Figure 7. Melting interface propagation for Cases 1–9.

Subsequently, Cases 4–6 are scrutinized, with an increased number of fins in this case grouping to reduce the negative influence of the bottom region in three other cases, namely Cases 1–3. At 780 s, there is still a big portion of solid PCM to be melted on the inner side (Case 6), whereas the outer PCM has split into smaller regions. Progressing to t = 1200 s, the temperature distribution of PCM in Case 6 appears relatively uniform, with only the PCM at the bottom demonstrating a lower temperature. The extended curved fin reaching the bottom of the PCM accelerates the melting speed of challenging-to-melt areas. By t = 1500 s, Case 6 completes the melting process, with the increased number of fins exerting a more pronounced warming effect on the PCM. Finally, Cases 7–9 are examined, indicating that the fin radius and the fin number in Cases 1–6 significantly affect the melting time. In this case grouping, Case 9 features a 40 mm radius for annular fins and 8 curved fins. Compared to the original situation, namely Case 1, the full melting time reduces from

9485 s to 1166 s, marking an 87.71% increase in melting rate. Through comparative analysis of the melting performance across varying cases, it is determined that the manipulation of the fin number and radius significantly enhances heat exchange efficiency and diminishes challenging-to-melt areas.

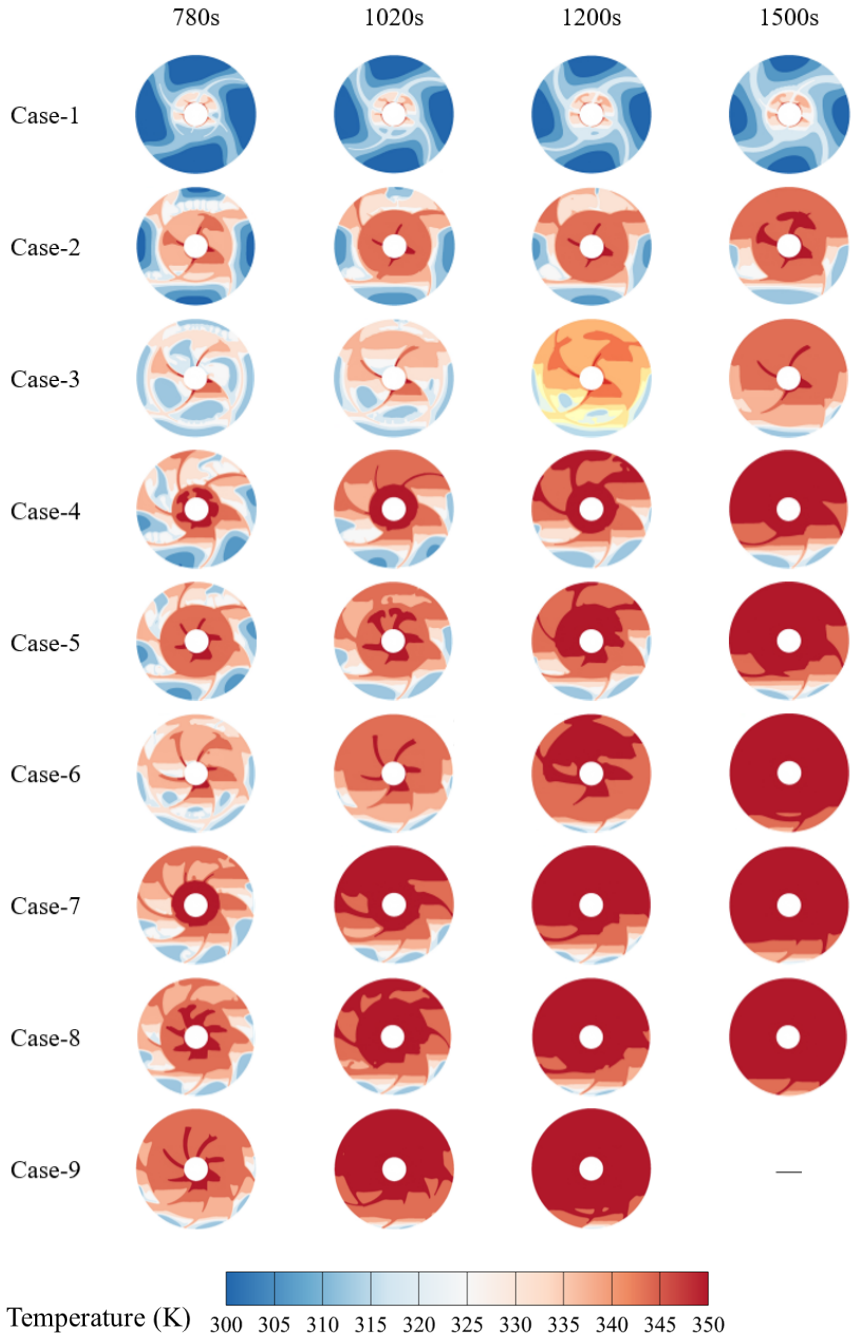

Figure 8. Temperature distribution for Cases 1–9.

The velocity field shown in Figure 9 for all cases reveals that the natural convection generated by the fins primarily concentrates in the upper segments of the fins, resulting in stronger buoyancy-induced flow in the upper region compared to the lower part across Cases 1–9. In Case 1, the most intense internal natural convection occurs at t = 780 s, gradually subsiding as the melting process nears completion at t = 1200 s, where natural convection mainly concentrates near the solid–liquid phase PCM. At this stage, natural convection weakens, and the melting of low-temperature PCM primarily relies on solid–

liquid PCM for heat transfer. In Case 9, the increased number of curved fins and expanded radius of annular fins at t = 780 s enhance the natural convection impact in the unit's lower region, resulting in a stronger heat transfer uniformity than those among the other eight cases. By t = 1020 s, Case 9 enters the last period of melting, with free convective flow primarily existing at the top. Upon reaching t = 1200 s, Case 9 completes the melting process, causing natural convection to nearly approach 0.

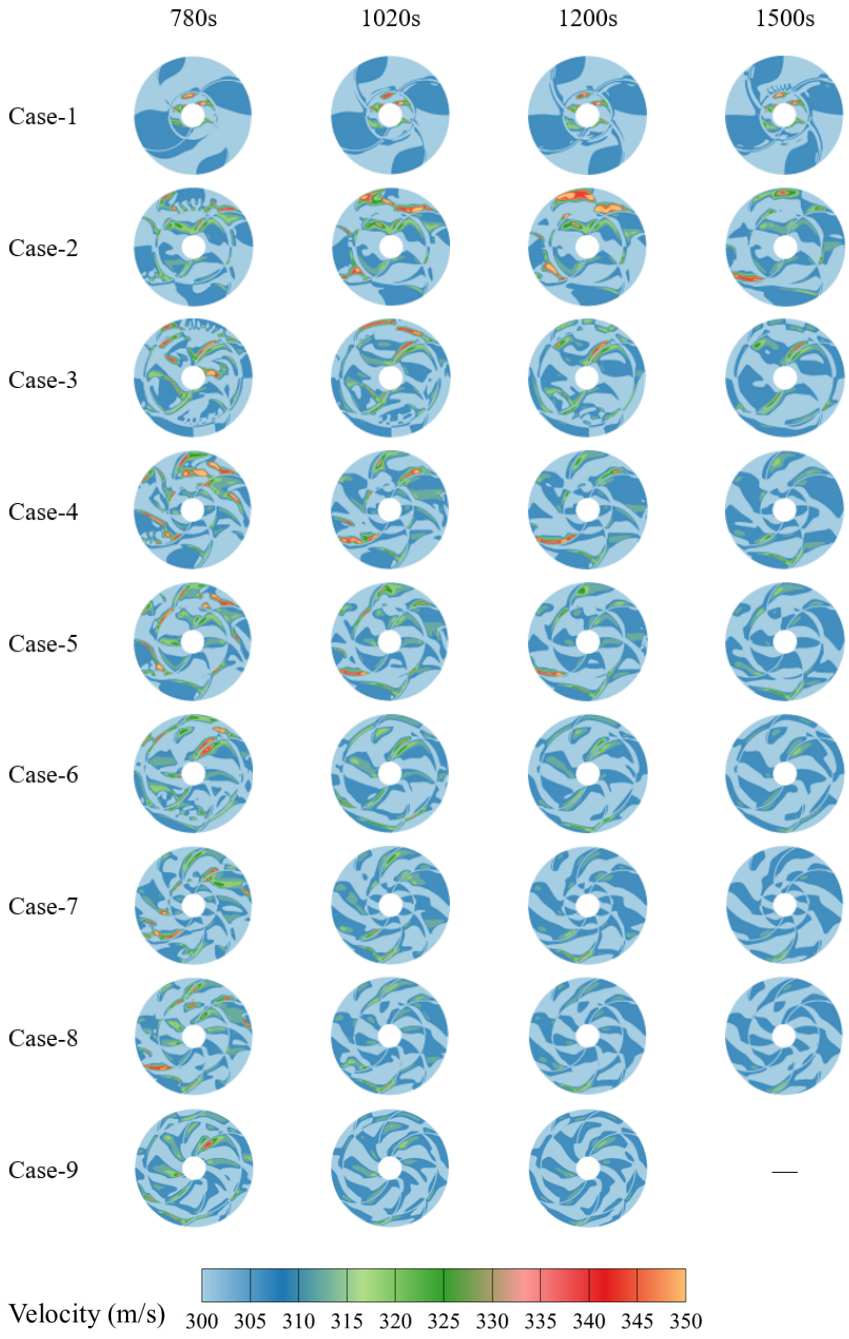

Figure 9. Velocity distribution in Cases 1–9 at different times.

4.2. Melting Fraction and Temperature Field

The analysis presents the melting fraction and the PCM average temperature for all cases. Examining the liquid phase rate change trend from Figure 10a, the liquid phase rate of Cases 1–3 initially rose slowly, indicating an inefficient melting process. Particularly for Case 1, the gradual increase in melting fraction reflects a slow melting speed due to a small annular fin radius and limited curved fins, resulting in reduced fin heat transfer efficiency.

Conversely, Cases 4–6, with an increased annular fin radius and additional curved fins, experience enhanced heat transfer capabilities. Furthermore, Cases 7–9 substantially improve the melting effect on the refractory zone by augmenting the annular fin radius and the number of curved fins. These design enhancements lead to a faster rate of liquid phase change in the initial phase, with the retardation of bottom PCM diminishing later in the melting process compared to Cases 1–3.

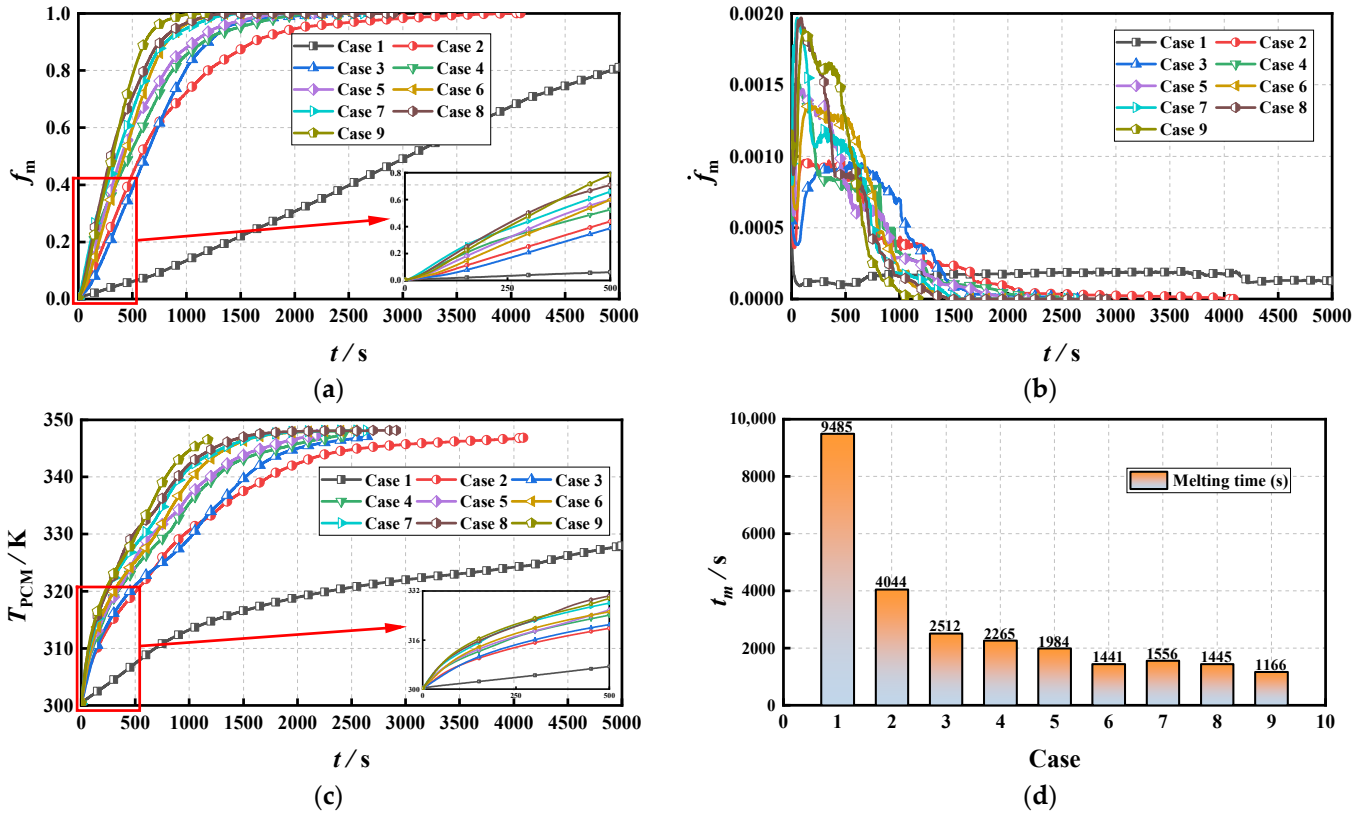

Figure 10. Descriptions of: (**a**) liquid fraction; (**b**) melting rate; (**c**) average temperature; (**d**) full melting time for all the cases.

Case 3 originally exhibits the greatest liquid fraction among the others due to its large annular fin radius, resulting in excellent initial melting performance. In contrast, Case 1, with its small annular fin radius and a limited number of curved fins, presents a slow increase in melting rate because of the retardation of the bottom PCM. The melting rates of the other eight cases follow a common trend: an initial peak in melting rate, a rapid decline, followed by an increase, and ultimately a gradual decrease over time. This phenomenon is primarily caused by the gradual weakening of natural convection during the melting process. Comparative analysis reveals that Case 9 reaches the greatest fraction of liquid PCM among the nine cases. Its melting fraction keeps a high increasing trend without the extended low melting rate stage observed in the later stage in Case 1 or Case 2, thus resulting in Case 9 having the shortest melting time. As shown in Figure 10c for the PCM mean temperature data, the change in PCM mean temperature is akin to the liquid phase rate trend. In the early period, Case 2 experiences the most rapid mean temperature change in PCM. At the mid-to-late stages of melting, the average temperature change rate of PCM decreases for Cases 1–6. Meanwhile, Case 9 exhibits a relatively stable temperature-rising trend throughout the entire process. During the middle/later stages of melting, Cases 1–6 mainly heat the challenging-to-melt PCM region, whereas Case 9 achieves a homogenized temperature distribution, allowing for a prolonged temperature-rising trend.

Comparing the melting times of Cases 1–9 as shown in Figure 10d, when the annular fin radius doubles, namely increasing from 20 mm to 40 mm, there is not a significant change in melting time in Cases 1–3. However, the comparison between Case 6 and Case 3 reveals that an increase in the number of fins leads to a 26.61% reduction in melting time. Likewise, in Case 9 compared to Case 3, the cross fins led to a 25.06% reduction in melting time. Notably, in the case of increasing the number of fins from four to eight, i.e., Case 9 compared to Case 3, there is a significant 41.22% reduction in melting time. Therefore, across different conditions of Cases 1–9, Case 9 exhibits the best melting efficiency. These findings indicate that increasing the fin number is beneficial for significantly reducing the melting time of PCHSS units, while further expanding the annular fins optimizes the melting performance.

4.3. Thermal Storage and Temperature Response

The changes in sensible heat and latent heat storage are examined in Figure 11a,b. Sensible heat denotes the heat absorbed as a substance's temperature increases without undergoing a phase transition, indicating a change in the average temperature. On the other hand, latent heat involves heat absorption during a phase transition, keeping the substance's temperature constant until the transition is complete, and is associated with the liquid ratio of PCM in the PCHSS. The variation in sensible heat storage correlates with the mean temperature change in PCM as depicted in Figure 10c. Adjusting the position and increasing the number of fins leads to a modification in PCM volume, thereby affecting the trends in latent heat absorption, reflecting the liquid proportion. The total latent heat absorption differs among various cases, with Case 4 demonstrating the highest total sensible heat storage due to the higher internal PCM temperature, while Case 1 exhibits the highest total latent heat storage owing to the lowest fin mass. Although Case 9's total energy storage is slightly lower than that of Case 1, this minor energy loss is deemed acceptable as it significantly extends the melting time. Moreover, the progression of total thermal energy over time is depicted in Figure 11c, indicating that sensible heat storage contributes to around 50% of the total absorption, suggesting that changes in total latent heat are primarily influenced by latent heat storage, as highlighted in Figure 11e.

Figure 11d,f illustrates the instantaneous and average heat storage rates across different scenarios. In all nine instances, the instantaneous heat storage rate peaks initially before gradually declining. At approximately 250 s, six cases show an upsurge in heat storage due to the combined effect of the annular fin and curved fin, enhancing heat absorption. Case 3 and Case 4 exhibit significant heat absorption rates during the initial melting phase, while Case 9 demonstrates the highest rate in the middle and late stages, persisting until the end of the melting process. Compared to Case 2, Case 3 and Case 5 experience a 37.85% and 50.89% increase in average heat absorption rates, respectively, while Case 4 shows a 35.91% increase from Case 3. Case 9, with the most effective melting performance, records an 88.06% increase in mean heat storage compared to Case 1, showcasing a remarkable improvement in heat absorption efficiency.

In addition to parameters such as rates of liquid phase and heat storage, this study also delves into temperature response to further investigate the thermal storage capabilities. It encompasses the use of instantaneous manipulations on response rates of temperature ($\dot{RR}$) and average temperature ($\overline{\dot{RR}}$), taking the form of [51]:

$$\dot{RR} = \int_0^{\dot{t_m}} \frac{1}{\dot{t_m}} \frac{T(t_i) - T(t_{i-1})}{t_i - t_{i-1}} dt \tag{19}$$

$$\overline{RR} = \int_0^{t_m} \frac{1}{t_m} \frac{T(t_i) - T(t_{i-1})}{t_i - t_{i-1}} dt \tag{20}$$

where t_m denotes the full melting time, $T(t_i)$ and $T(t_{i-1})$ represent the temperatures at t_i and t_{i-1}, respectively.

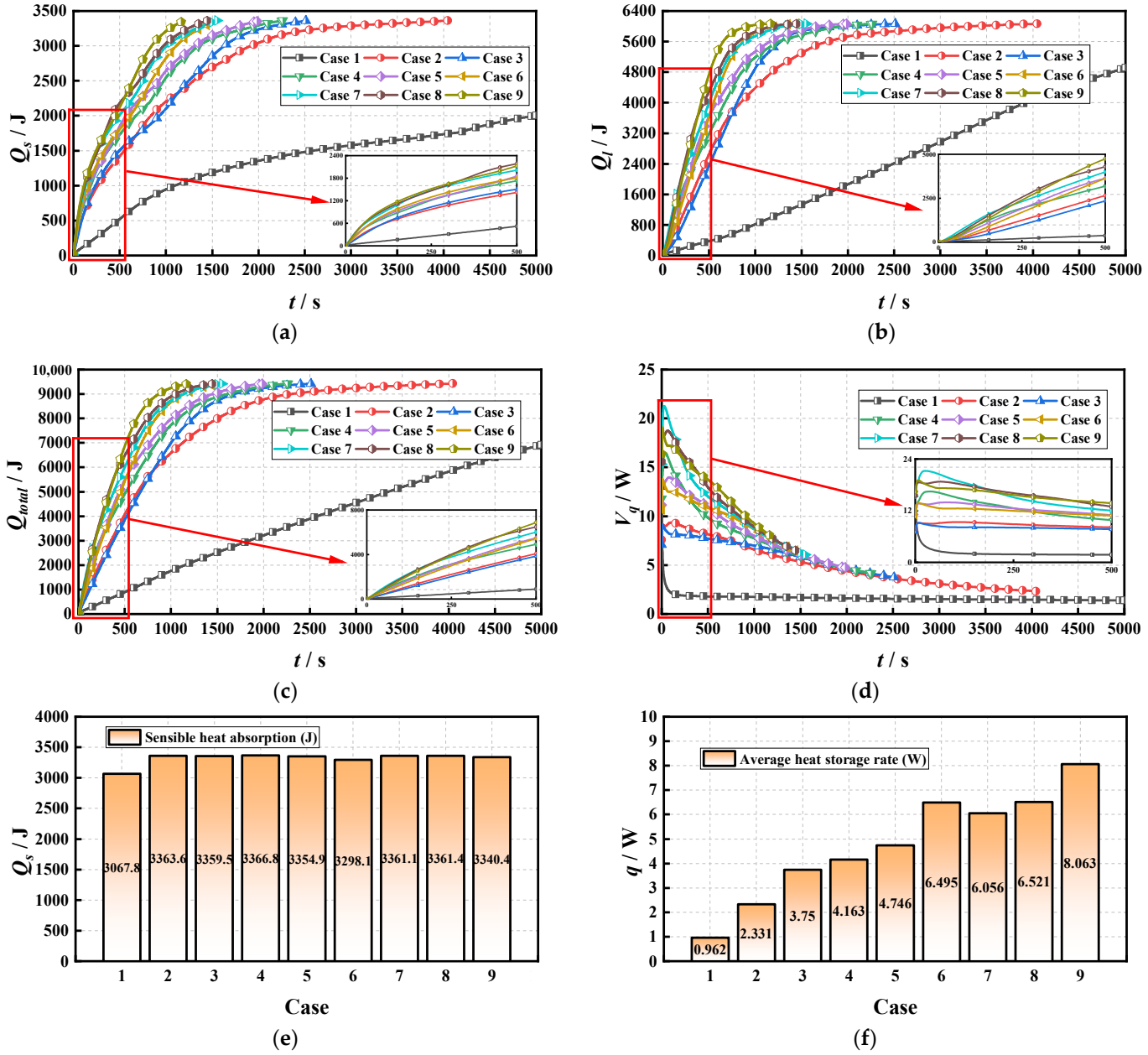

Figure 11. Descriptions of: (**a**) sensible heat storage; (**b**) latent heat storage; (**c**) total heat storage; (**d**) heat storage rate; (**e**) ending heat storage; (**f**) average heat storage rate for all the cases.

In Figure 12a, a plot of the instantaneous temperature changes occurring over time for nine different scenarios is displayed. The figure reveals that the instantaneous temperature response in all cases experiences a rapid rise from zero to a peak initially, followed by a gradual decline. During this period, Case 2 and Case 3 exhibit higher instantaneous temperature responses, while in the middle and late phases of melting, Case 9 demonstrates the highest response, persisting until the conclusion of the melting procedure. Figure 12b facilitates quantitative comparisons of the mean temperature response for different scenarios. Upon comparison, it is found that the average temperature responses of Case 2 and Case 3 exceed that of the base case (Case 1) by 6.86% and 66.28%, respectively. Furthermore, the increment

in fin number, from Case 7 to Case 9, led to a 54% increase in the average temperature response. Additionally, expanding the annular fins, as in the transition from Case 5 to Case 6, resulted in a 30.3% augmentation in the average temperature response. Across all cases, Case 9 exhibited the most effective melting performance, with its average temperature response increasing by 87.84% compared with Case 1, highlighting its substantial impact on improving temperature response.

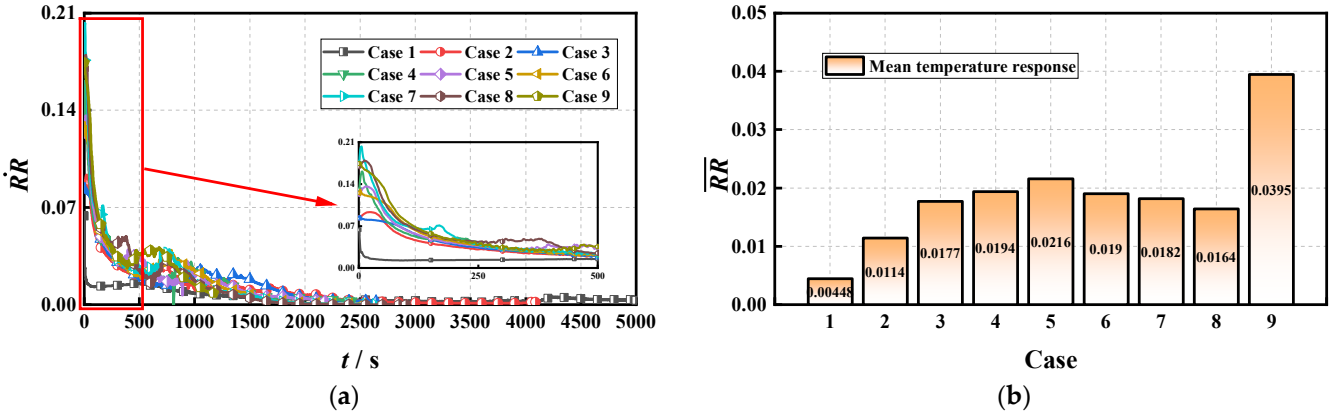

Figure 12. Descriptions on temperature responses of: (**a**) instantaneous and (**b**) average manipulation.

4.4. Dynamic Temperature Study

In this section, the internal position temperature monitoring of Case 1 and Case 9 is used to prove the melting performance improvement effect of Case 9. Figure 13 shows the internal location selection for Case 1 and Case 9.

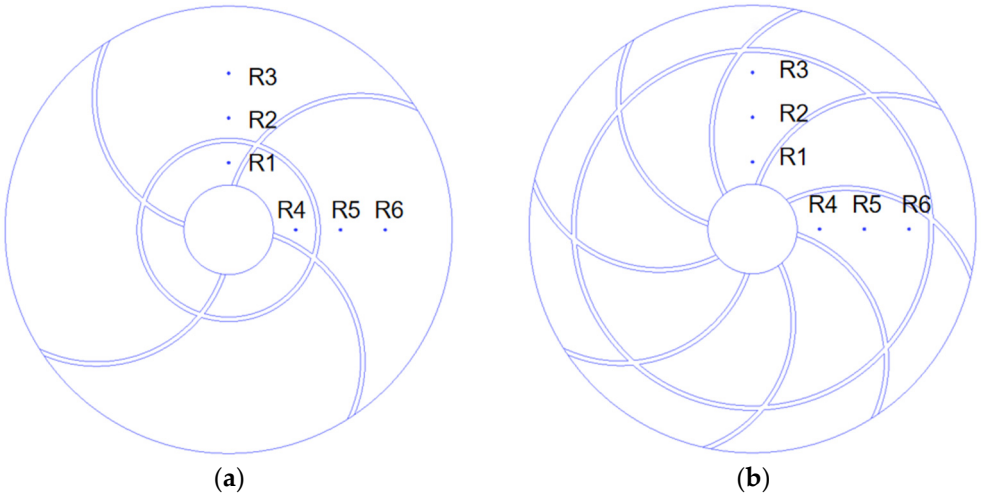

Figure 13. Comparison of: (**a**) Case 1 system internal point settings; (**b**) Case 9 system internal point settings.

As the location point moves away from the heat source, the temperature gradually decreases, as shown in Figure 14a,b. The configuration of the ring and curved fins in Case 9 brings the heat transfer section closer to all points, resulting in a higher temperature than in Case 1. Conversely, points 4, 5, and 6 in the horizontal position within the PCM show higher temperatures compared to points in the vertical position. In Case 9, due to the short melting period and uniform temperature distribution at all points, at t = 1000 s, the melting process enters the final stage. Therefore, the increase in the radius and number of annular fins increases the refractory area, improves the heat transfer efficiency, and shortens the melting time.

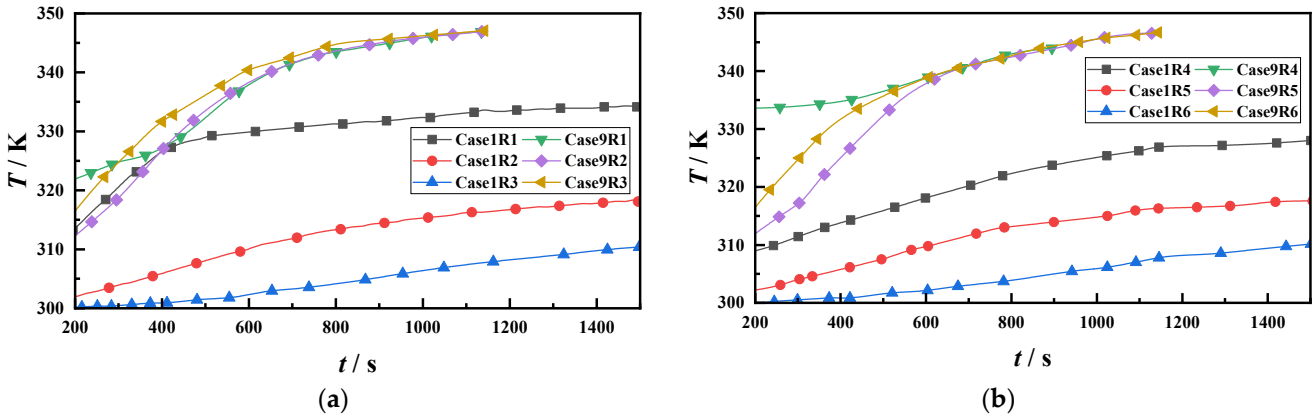

Figure 14. Comparison of: (**a**) Temperature comparison between Case 1 and Case 9 at points 1, 2, and 3; (**b**) Temperature comparison between Case 1 and Case 9 at points 4, 5, and 6.

5. Conclusions

To integrate phase change heat storage into building heating and hot-water production systems, this paper adopts a composite fin design combining a circular fin and rectangular fins to improve overall heat storage performance. The main conclusions are as follows:

(1) The presence of a refractory zone at the bottom of the terminal unit will significantly reduce the heat transfer rate and extend the time required for complete melting;

(2) The increase in the radius of circular fins and the number of curved fins at the same time is conducive to natural convection. Compared with the initial structure design (four curved fins and 20 mm radius round fins), the structural design Case 9 (eight curved fins and 40 mm radius round fins) can greatly improve the heat storage rate;

(3) The dynamic temperature response analysis shows that the area of the refractory zone can be reduced by increasing the radius and number of annular fins, and the average temperature response of Case 9 is increased by 781.25% compared with the initial structure;

(4) In future research, the radius of the annular fin can be further optimized and the bending degree of the curved fin can be considered under the premise of considering the feasibility of engineering application.

Author Contributions: Conceptualization, Q.C. and C.W.; methodology, T.N.; software, C.H.; validation, J.S., Q.C. and T.N.; formal analysis, Q.C.; investigation, C.H.; resources, J.S.; data curation, J.S.; writing—original draft preparation, Q.C.; writing—review and editing, J.S.; visualization, C.H.; supervision, J.S.; project administration, J.S.; funding acquisition, Q.C. All authors have read and agreed to the published version of the manuscript.

Funding: This research was funded by the Natural Science Foundation of Shaanxi Province (No. 2024JC-YBQN-0343).

Data Availability Statement: The original contributions presented in the study are included in the article, further inquiries can be directed to the corresponding author.

Conflicts of Interest: The authors declare no conflicts of interest.

Nomenclature

PCM	Phase change material
LHTES	Latent heat thermal energy storage
HTF	Heat transfer fluid
HWODS	Hot-water oil displacement system

Symbols	
A_{mush}	Velocity momentum in the paste region
k	Thermal conductivity (W/m·K)
ρ	Density (kg/m^3)
c_p	Isobaric specific heat (J/kg·K)
T_m	Melting temperature (K)
λ	Latent heat of fusion (J/kg)
β	Volumetric coefficient of thermal expansion (K^{-1})
T_s	Solidus temperature (K)
T_l	Liquidus temperature (K)
f_m	Liquid fraction
$\dot{f}_m$	Melting rate
h	Total enthalpy (J)
Q_s	Sensible heat energy (J)
Q_l	Latent heat energy (J)
Q	Total heat energy (J)
$\dot{q}$	Instantaneous heat absorption rate (W)
$\overline{q}$	Average heat absorption rate (W)
$\dot{RR}$	Instantaneous temperature response rate
$\overline{RR}$	Average temperature response rate
Subscripts	
w	wall
s	solid phase
l	liquid phase
Ω	heat transfer area
ref	reference state

References

1. Cho, K.-H.; Chen, C.-Y.; Aguda, A.; Fournier, M.J.; Su, X. Toward sustainable electrochemically mediated separations driven by renewable energy. *Joule* **2024**, *8*, 3259–3280. [CrossRef]
2. Keomeesay, P.; Liu, N.; Nie, Y.; Li, S.; Zhang, W.; Liu, Y.; Souliyathai, D.; Li, X.; Chen, Y.; Zhao, X.; et al. Review of the Lao People's Democratic Republic energy policies for sustainable development. *Energy Convers. Manag.* **2025**, *324*, 119327. [CrossRef]
3. Amin, M.; Hussain Shah, H.; Azhar Iqbal, M. Barriers to sustainable hydrogen production through renewable energy processes and their environmental impacts. *Sustain. Energy Technol. Assess.* **2024**, *72*, 104075. [CrossRef]
4. Lahoud, C.; Chahwan, A.; Rishmany, J.; Yehia, C.; Daaboul, M. Enhancing Energy Efficiency in Mediterranean Coastal Buildings Through PCM Integration. *Buildings* **2024**, *14*, 4023. [CrossRef]
5. Pinamonti, M.; Baggio, P. Energy and economic optimization of solar-assisted heat pump systems with storage technologies for heating and cooling in residential buildings. *Renew. Energy* **2020**, *157*, 90–99. [CrossRef]
6. Huang, X.; Zhou, R.; Luo, X.; Yang, X.; Cheng, J.; Yan, J. Experimental research and multi-physical modeling progress of Zinc-Nickel single flow battery: A critical review. *Adv. Appl. Energy* **2023**, *12*, 100154. [CrossRef]
7. Zhang, J.; Lin, Y.; Wang, L.; Wang, Q.; Zhu, K.; Yang, S.; Guo, G. Research and Case Application of Zero-Carbon Buildings Based on Multi-System Integration Function. *Buildings* **2024**, *14*, 3394. [CrossRef]
8. Ding, Z.; Sui, Y.; Zhai, C.; Sui, Z.; Lin, H.; Li, F.; Wu, W. Transient supply-demand matching and numerical parametric study of solar absorption thermal battery for space cooling. *Energy Convers. Manag.* **2023**, *288*, 117177. [CrossRef]
9. Rehman, H.U.; Nik, V.M.; Ramesh, R.; Ala-Juusela, M. Quantifying and Rating the Energy Resilience Performance of Buildings Integrated with Renewables in the Nordics under Typical and Extreme Climatic Conditions. *Buildings* **2024**, *14*, 2821. [CrossRef]
10. Sui, Y.; Lin, H.; Ding, Z.; Li, F.; Sui, Z.; Wu, W. Compact, efficient, and affordable absorption Carnot battery for long-term renewable energy storage. *Appl. Energy* **2024**, *357*, 122504. [CrossRef]
11. Xu, D.; Qu, Z.; An, L.; Xu, H.; Yang, Q.; Luo, Z.; Pan, H. Pore-scale study on the effects of randomly distributed void cavities on the thermal performance of composite phase change materials. *J. Energy Storage* **2022**, *55*, 105715. [CrossRef]
12. Zhang, C.; Li, D.; Wang, L.; Zhang, S.; Shen, C.; Gao, R. A real-time controllable pressure-driven smart window with Cu^{2+} solution. *Energy Build.* **2025**, *329*, 115236. [CrossRef]
13. Ding, Z.; Wu, W. A phase-change-material-assisted absorption thermal battery for space heating under low ambient temperatures. *Energy* **2024**, *299*, 131407. [CrossRef]

14. Elmnefi, M.; Al-Khazraji, W. Numerical and experimental studies of thermal performance enhancement for parabolic trough solar collector using none-circulated CuO/synthetic oil nanofluid. *Int. J. Numer. Methods Heat Fluid Flow* **2023**, *33*, 3124–3163. [CrossRef]
15. Zhang, W.; Ding, J.; Yin, S.; Zhang, F.; Zhang, Y.; Liu, Z. Thermo-economic optimization of an artificial cavern compressed air energy storage with CO_2 pressure stabilizing unit. *Energy* **2024**, *294*, 130821. [CrossRef]
16. Li, S.; Cheng, Y.Z.; Shen, Q.W.; Wang, C.Y.; Peng, C.D.; Yang, G.G. Numerical analysis on the thermal management of phase change material with fins for lithium-ion batteries. *Int. J. Numer. Methods Heat Fluid Flow* **2024**, *34*, 1170–1188. [CrossRef]
17. Yan, H.; Luo, L.; Zhang, J.F.; Du, W.; Huang, D.; Wang, S.T. Numerical analysis of heat transfer characteristics in a pin fin-dimpled channel with different pin fins and dimple locations. *Int. J. Numer. Methods Heat Fluid Flow* **2022**, *32*, 3132–3158. [CrossRef]
18. Xu, H.J.; Wang, Y.; Han, X.C. Analytical considerations of thermal storage and interface evolution of a PCM with/without porous media. *Int. J. Numer. Methods Heat Fluid Flow* **2020**, *30*, 373–400. [CrossRef]
19. Yang, B.; Guo, J.; Huang, X.; Li, Z.; Yang, X.; Li, M.-J. Evaluation of variable rotation on enhancing thermal performance of phase change heat storage tank. *Int. J. Heat Fluid Flow* **2024**, *106*, 109328. [CrossRef]
20. Park, S.; Jo, B. Novel surfactant-free microencapsulation of molten salt using TiO_2 shell for high temperature thermal energy storage: Thermal performance and thermal reliability. *J. Energy Storage* **2023**, *63*, 107016. [CrossRef]
21. Huang, Y.; Stonehouse, A.; Abeykoon, C. Encapsulation methods for phase change materials—A critical review. *Int. J. Heat Mass Transf.* **2023**, *200*, 123458. [CrossRef]
22. Zhang, P.; Cheng, Z.; Chen, Z.; Gao, Y. Oleophobic modification of clay minerals to improve encapsulation ratios of shape-stabilized phase change materials: A universal method. *Prog. Nat. Sci. Mater. Int.* **2021**, *31*, 904–910. [CrossRef]
23. Liu, L.; Zhang, X.; Liang, H.; Niu, J.; Wu, J.-Y. Cooling storage performance of a novel phase change material nano-emulsion for room air-conditioning in a self-designed pilot thermal storage unit. *Appl. Energy* **2022**, *308*, 118405. [CrossRef]
24. Ergün, A.; Eyinç, H. Performance assessment of novel photovoltaic thermal system using nanoparticle in phase change material. *Int. J. Numer. Methods Heat Fluid Flow* **2019**, *29*, 1490–1505. [CrossRef]
25. Xu, Y.; Zheng, Z.-J.; Yang, C.; Cai, X. Intelligent optimization of horizontal fins to improve the melting performance of phase change materials in a square cavity with isothermal vertical wall. *J. Energy Storage* **2021**, *44*, 103334. [CrossRef]
26. Chen, D.; Riaz, A.; Aute, V.C.; Radermacher, R. Comprehensive performance analysis and structural improvement of latent heat thermal energy storage (LHTES) unit using a novel parallel enthalpy-based lattice Boltzmann model. *J. Energy Storage* **2023**, *73*, 108902. [CrossRef]
27. Li, Z.-R.; Hu, N.; Fan, L.-W. Nanocomposite phase change materials for high-performance thermal energy storage: A critical review. *Energy Storage Mater.* **2023**, *55*, 727–753. [CrossRef]
28. Guo, C.; Lan, M.; Li, M.; Tang, S.; Zhang, D.; Song, J.; Li, H. Studying the advantages of equal curvature curved fin to enhance phase change heat storage. *J. Energy Storage* **2023**, *57*, 106212. [CrossRef]
29. Xu, Y.; He, C.; Chen, Y.; Sun, Y.; Yin, H.; Zheng, Z.-J. Experimental and numerical study on the effect of the intelligent memory metal fin on the melting and solidification process of PCM. *Renew. Energy* **2023**, *218*, 119366. [CrossRef]
30. Boujelbene, M.; Mohammed, H.I.; Sultan, H.S.; Eisapour, M.; Chen, Z.; Mahdi, J.M.; Cairns, A.; Talebizadehsardari, P. A comparative study of twisted and straight fins in enhancing the melting and solidifying rates of PCM in horizontal double-tube heat exchangers. *Int. Commun. Heat Mass Transf.* **2024**, *151*, 107224. [CrossRef]
31. Mills, T.; Venkateshwar, K.; Tasnim, S.H.; Mahmud, S. Numerical and experimental investigation of the melting of a PCM in an enclosure having a tree-shaped internal fin. *Therm. Sci. Eng. Prog.* **2024**, *48*, 102434. [CrossRef]
32. Unnikrishnan, K.S.; Santhosh, K.; Rohinikumar, B. Experimental and numerical analysis of PV-PCM integrated with novel shaped corrugated fins. *Therm. Sci. Eng. Prog.* **2024**, *50*, 102562. [CrossRef]
33. Han, X.; Liu, S.; Zeng, C.; Yang, L.; Shukla, A.; Shen, Y. Investigating the performance enhancement of copper fins on trapezoidal thermochemical reactor. *Renew. Energy* **2020**, *150*, 1037–1046. [CrossRef]
34. Guedri, K.; Singh, P.; Riaz, F.; Inayat, A.; Shah, N.A.; Fadhl, B.M.; Makhdoum, B.M.; Arsalanloo, A. Solidification acceleration of phase change material in a horizontal latent heat thermal energy storage system by using spiral fins. *Case Stud. Therm. Eng.* **2023**, *48*, 103157. [CrossRef]
35. Liu, Y.; Chen, Y.-X.; Zhang, M.; Zhao, X.; Li, T. Enhanced thermal performance of shell and tube phase change heat accumulator with novel biomimetic spider web fins. *Appl. Therm. Eng.* **2023**, *233*, 121224. [CrossRef]
36. Huang, X.; Li, F.; Xiao, T.; Li, Y.; Yang, X.; He, Y.-L. Structural optimization of melting process of a latent heat energy storage unit and application of flip mechanism. *Energy* **2023**, *280*, 128164. [CrossRef]
37. Mao, Q.; Li, Y.; Li, G.; Badiei, A. Study on the influence of tank structure and fin configuration on heat transfer performance of phase change thermal storage system. *Energy* **2021**, *235*, 121382. [CrossRef]
38. Kirincic, M.; Trp, A.; Lenic, K. Numerical evaluation of the latent heat thermal energy storage performance enhancement by installing longitudinal fins. *J. Energy Storage* **2021**, *42*, 103085. [CrossRef]

39. Al-Mudhafar, A.H.N.; Nowakowski, A.F.; Nicolleau, F.C.G.A. Enhancing the thermal performance of PCM in a shell and tube latent heat energy storage system by utilizing innovative fins. *Energy Rep.* **2021**, *7*, 120–126. [CrossRef]
40. Modi, N.; Wang, X.; Negnevitsky, M. Melting and solidification characteristics of a semi-rotational eccentric tube horizontal latent heat thermal energy storage. *Appl. Therm. Eng.* **2022**, *214*, 118812. [CrossRef]
41. Al-Abidi, A.A.; Mat, S.; Sopian, K.; Sulaiman, M.Y.; Mohammad, A.T. Experimental study of PCM melting in triplex tube thermal energy storage for liquid desiccant air conditioning system. *Energy Build.* **2013**, *60*, 270–279. [CrossRef]
42. Nie, C.; Deng, S.; Liu, J.; Rao, Z. Nonuniform concentrated nanoparticles enhancing melting of phase change materials in vertical shell-tube storage unit with annular fins. *J. Energy Storage* **2023**, *72*, 108254. [CrossRef]
43. Safari, V.; Kamkari, B.; Hooman, K.; Khodadadi, J.M. Sensitivity analysis of design parameters for melting process of lauric acid in the vertically and horizontally oriented rectangular thermal storage units. *Energy* **2022**, *255*, 124521. [CrossRef]
44. Huang, X.; Li, Y.; Lu, L.; Gao, X.; Yang, X.; Li, M.-J. Numerical investigations on heat release performance of phase change mixture of paraffin and water. *Sol. Energy Mater. Sol. Cells* **2025**, *280*, 113266. [CrossRef]
45. Xu, H.; Wang, N.; Zhang, C.; Qu, Z.; Cao, M. Optimization on the melting performance of triplex-layer PCMs in a horizontal finned shell and tube thermal energy storage unit. *Appl. Therm. Eng.* **2020**, *176*, 115409. [CrossRef]
46. Singh, V.K.; Patel, A. Effect of mushy zone constant on the melting of a solid-liquid PCM under hyper-gravity conditions. *Int. Commun. Heat Mass Transf.* **2022**, *134*, 105993. [CrossRef]
47. Huang, X.; Hu, R.; Gao, X.; Yang, X.; Li, M.-J. Study on melting process of latent heat energy storage system by nano-enhanced phase change material under rotation condition. *Appl. Therm. Eng.* **2024**, *247*, 123040. [CrossRef]
48. Khan, J.; Nithyanandam, K.; Singh, P. Computational study on transient thermal performance enhancement of phase change materials in triplex tube heat exchanger through novel annular-finned configurations. *Numer. Heat Transf. Part A Appl.* **2024**, 1–18. [CrossRef]
49. Zhang, Y.; Yang, X.; Zou, S.; Xu, X.; Tu, Y.; Tian, Y.; Ke, Z. Enhancing the phase change material based shell-tube thermal energy storage units with unique hybrid fins. *Int. Commun. Heat Mass Transf.* **2024**, *157*, 107763. [CrossRef]
50. Al-Abidi, A.A.; Mat, S.; Sopian, K.; Sulaiman, M.Y.; Mohammad, A.T. Experimental study of melting and solidification of PCM in a triplex tube heat exchanger with fins. *Energy Build.* **2014**, *68*, 33–41. [CrossRef]
51. Huang, X.; Liu, Z.; Gao, X.; Xie, Y.; Gao, J.; Yang, X. Application of actively enhanced solar phase change heat storage system in building heating: A numerical and statistical optimization study. *Renew. Energy* **2025**, *241*, 122328. [CrossRef]